**1**  **Mixing state, spatial distribution, sources and**

**2**  **photochemical enhancement to sulfate formation of black**

**3**  **carbon particles in the Arctic Ocean during summer**

4

5  Longquan Wang[1,2], Jinpei Yan[3], Afeng Chen[1,4], Bei Jiang[1,5], Fange Yue[1], Xiawei Yu[1],

6  Zhouqing Xie[1,6*]

7

8  [1]Anhui Key Laboratory of Polar Environment and Global Change, Department of Environmental Science

9  and Engineering, University of Science and Technology of China, Hefei 230026, China.

10  [2]Department of Carbon Neutral Science and Engineering, Anhui University of Science and Technology,

11  Hefei 230026, China.

12  [3]Third Institute of Oceanography, Ministry of Natural Resources, Xiamen 361005, China.

13  [4]Engineering and Technological Research Centre of National Disaster Relief Equipment, Army Logistics

14  Academy, Chongqing, 401331, China.

15  [5]College of Ecology and Environment, Xinjiang University, Urumqi, 830017, PR China.

16  [6]State Key Laboratory of Fire Science, University of Science and Technology of China, Hefei, 230026,

17  China.

18  *Correspondence to*: Zhouqing Xie (zqxie@ustc.edu.cn)

**Abstract.** Black carbon heats the atmosphere by absorbing solar radiation and regulates the radiation

balance of the Earth. Specifically in the Arctic region, black carbon accelerates Arctic warming by

simultaneously altering surface albedo. Nonetheless, assessing the climatic impacts of black carbon

aerosols in the Arctic is challenging due to their considerable variability in temporal and spatial

distribution, sources, and chemical composition. Black carbon particles (0.2-2μm) in the Arctic Ocean

were investigated using a ship-based single particle aerosol mass spectrometer from July to August 2017.

In the central Arctic Ocean, near the Norwegian Sea-Iceland and the North Atlantic, biomass combustion

is the predominant source of black carbon particles, constituting over 50%, with a particularly high

contribution exceeding 70% in the central Arctic Ocean. Within the Chukchi Sea region, terrestrial

transport from mid and low latitudes emerges as the primary source of black carbon particles,

representing over 50%, with biomass combustion and anthropogenic pollution sources each contributing

around 25%. Near Svalbard, biomass combustion sources and terrigenous transport stand out as the

primary sources of black carbon particles, with their contributions being comparable. Furthermore, the

ratio of sulfate to nitrate in black carbon particles was notably higher compared to that in sea salt particles.

This ratio increased with elevated black carbon content and sunlight intensity, suggesting that Arctic

black carbon particles substantially facilitated sulfate formation through photochemical processes. Such

interactions could potentially modify the mixing state of Arctic black carbon particles and their radiative

impacts.

## 1   Introduction

Black carbon, an amorphous form of carbon produced by the incomplete combustion of carbon-

containing fuels or biomass, plays a crucial role in atmospheric physical chemistry by absorbing solar

radiation and influencing Earth's radiation balance. Additionally, the warming effect of black carbon

modifies the vertical stability of the atmosphere and alters cloud distribution, which further impacts the

radiation balance (Ramanathan & Carmichael, 2008). The deposition of black carbon on ice and snow

surfaces significantly reduces their albedo, accelerating the melting process. This is particularly

pronounced in the Arctic region, where black carbon contributes to warming not only by heating the

atmosphere but also by changing the surface albedo and through other direct and indirect radiative effects

(Flanner et al., 2007; Serreze & Barry, 2011). Arctic black carbon aerosol, characterized as a transportable

48    species with various potential sources, exhibits distinct spatial and seasonal distribution patterns (Matsui

49    et al., 2022). These variations are critical for assessing its impact on radiative forcing. Furthermore, the

50    mixing state of particles containing black carbon significantly influences their radiative effects (Jacobson,

51    2001), making detailed observations and analyses essential.

52    The mass concentration of black carbon aerosols in the Arctic near-surface atmosphere exhibits

53    significant seasonal variability, typically higher in winter and spring, and lower in summer and autumn

54    (Qi et al., 2017; Sharma et al., 2006; Sharma et al., 2004; Sharma et al., 2019). Influenced by atmospheric

55    transport patterns, the sources and vertical structures of black carbon aerosols also vary seasonally.

56    During winter and spring, the Arctic near-surface atmosphere is predominantly affected by transport from

57    higher latitudes, facilitating the movement of black carbon from Siberia and Europe through low-altitude

58    pathways to the bottom of the Arctic troposphere. Conversely, black carbon from mid-latitudes reaches

59    the middle and upper troposphere of the Arctic via long-distance transport. In summer, increased

60    precipitation in middle and high latitudes, which impedes long-distance transport, shifts the primary

61    source of atmospheric black carbon to biomass burning within the Arctic and neighboring regions such

62    as Siberia and Alaska (Evangeliou et al., 2016; Matsui et al., 2022; Wang et al., 2014). Although

63    atmospheric concentrations of black carbon are lower in summer than in winter, the higher frequency of

64    summer precipitation leads to quicker removal rates and higher deposition fluxes of atmospheric black

65    carbon (Willis et al., 2018). Observational data on atmospheric black carbon aerosol concentrations in

66    the Arctic also demonstrate notable spatiotemporal variations. Long-term continuous measurements at

67    Barrow and Alert stations in the Arctic revealed that the average concentration of black carbon aerosols

68    from 1980 to 2003 was approximately 25 ng/m³ (Sharma et al., 2004). Meanwhile, the average annual

69    concentration measured at Zeppelin Station from 1998 to 2007 was 39 ng/m³ (Eleftheriadis et al., 2009),

70    significantly higher than the former. Additionally, the spatial distribution of black carbon in Arctic ice

71    and snow varies, with concentrations decreasing from the Russian Arctic, through the Canadian and

72    Alaskan Arctic, to the Arctic Ocean and Greenland, highlighting a significant decline from the Arctic

73    coastal regions to the central Arctic Ocean (Dou & Xiao, 2016). These temporal and spatial discrepancies

74    in Arctic black carbon aerosols underline the importance of long-term, multi-regional observations in the

75    Arctic.

76    Evaluating the climatic impact of black carbon aerosols in the atmosphere and on snow cover is

77 crucial for understanding Arctic climate change. Unlike greenhouse gases such as carbon dioxide and

78 methane, black carbon aerosols possess a broader absorption spectrum, capable of absorbing radiation

79 across infrared to ultraviolet wavelengths (Bond & Bergstrom, 2006). In the IPCC 5th Assessment Report,

80 the direct radiative forcing of black carbon aerosols was estimated at 0.4 W/m^2, with a range of 0.05 to

81 0.8 W/m^2. The effective radiative forcing, which includes direct radiative impacts along with climate

82 feedbacks and rapid adjustments, was initially estimated at -0.45 ± 0.5 W/m^2. This estimate has since

83 been revised to 0.063 W/m^2, ranging from -0.28 to 0.42 W/m^2, reflecting a deeper understanding of

84 black carbon's effects on clouds and water vapor. Research indicates that the direct radiative forcing from

85 black carbon aerosols originating from fossil fuels is comparable to 78% of that from carbon dioxide,

86 while those from biomass burning equate to about 58% of carbon dioxide's effect (Hansen et al., 2005).

87 Considering indirect effects like changes in ice and snow albedo and cloud properties, the black and

88 organic carbon components from fossil fuel soot exert a net positive global radiative forcing. In contrast,

89 those from biomass combustion have a net negative global radiative forcing (Hansen et al., 2005). In the

90 Arctic, black carbon aerosols starkly contrast with the bright ice and snow surfaces, enhancing their solar

91 radiation absorption and leading to higher direct radiative forcing. Studies suggest that in the Arctic, the

92 warming effect of black carbon aerosols surpasses the cooling effect of reflective aerosols, making them

93 a potent warming agent in the region (Quinn et al., 2007). Beyond atmospheric warming, black carbon

94 in snow can intensify climate change by modifying the albedo feedback of snow and ice. The deposition

95 of black carbon on snow surfaces not only increases heat absorption but also, due to near-surface

96 temperature inversions that restrict energy dispersal in the Arctic, this absorbed heat further warms the

97 near-surface atmosphere. This process accelerates ice and snow melt and alters surface albedo, thereby

98 amplifying Arctic warming through the ice-albedo feedback mechanism, a significant factor in Arctic

99 amplification (Clarke & Noone, 1985; Dou & Xiao, 2016). The estimated annual mean radiative forcing

100 of black carbon aerosols from various sources on Arctic ice and snow is approximately 0.17 W/m^2 (Dou

101 & Xiao, 2016).

102     In the Arctic region, the mixing state of black carbon aerosols from different sources significantly

103 influences their radiative effects (Jacobson, 2001; Matsui et al., 2022). The internal mixing of black

104 carbon aerosols with scattering aerosols such as sulfate and organic carbon can substantially alter the

105 optical properties of black carbon, increasing its positive radiative forcing (Chung & Seinfeld, 2002). It

106  has been observed that anthropogenic black carbon aerosols from Asia generally have a thicker coating

107  compared to those from Europe, Siberia, and North America. This thicker coating is attributed to the

108  rapid aging of Asian aerosols upon emission, often accompanied by condensable gases. Moreover, Asian

109  anthropogenic black carbon typically travels at higher altitudes and over longer distances, resulting in a

110  longer residence time and more thorough aging process (Matsui et al., 2022). Black carbon aerosols of

111  different origins within the same region also exhibit variations in their mixing state. For instance, black

112  carbon aerosols from biomass combustion in Siberia and North America tend to have a larger proportion

113  and thicker coatings compared to those from anthropogenic sources in these areas. This difference is

114  largely due to the transport of biomass combustion-derived black carbon to the Arctic occurring primarily

115  in summer, which facilitates a faster aging rate than in winter (Matsui et al., 2022). Anthropogenic black

116  carbon from Asia and biomass-burning-derived black carbon aerosols from Siberia and North America

117  exhibit stronger positive radiative effects (Matsui et al., 2022). Additionally, the mixing state of black

118  carbon aerosols affects nucleation and wet clearance processes, thereby indirectly influencing their

119  radiative effects (Ching et al., 2012; Ching et al., 2018). These findings highlight that the source and

120  mixing state of Arctic black carbon aerosols represent key uncertainties in assessing their radiative

121  impacts, and that field observations are crucial for accurately evaluating their climate effects.

122       The condensation of secondary species like sulfate, nitrate, and organic matter on the surfaces of

123  black carbon particles significantly alters their mixing state (Ault et al., 2010). Despite this, few studies

124  have explored the secondary processes occurring on black carbon aerosol surfaces. Black carbon is

125  known to actively participate in some of these secondary processes. Recent laboratory research indicates

126  that black carbon may catalyze the formation of sulfate, significantly contributing to the growth of

127  secondary inorganic components in urban haze in China (Zhang et al., 2020). Research has also

128  demonstrated that black carbon aerosols are photoactive, capable of releasing reactive oxygen species,

129  including excited oxygen molecules and hydroxyl radicals, into the atmosphere. These species potentially

130  facilitate the formation of sulfate and organic matter (Gehling & Dellinger, 2013; Li et al., 2019). Further

131  studies have confirmed that black carbon aerosols engage in photochemical processes that enhance

132  sulfate generation in urban settings (Zhang et al., 2021). However, such studies have not yet been

133  extended to the Arctic region. Given the Arctic's sensitivity to climate changes influenced by aerosol

134  species like black carbon and sulfate, this potential photochemical process could introduce significant

135    uncertainties in assessing the local aerosol physicochemical properties and their radiative effects.

136

137    **2    Materials and Methods**

138    **2.1  Research region and instruments**

139         Observations were conducted aboard the R/V "Xuelong" during the 8th Chinese Arctic Expedition

140    Research Cruise, which traversed a significant portion of the Arctic Ocean, spanning from 56.2° to

141    84.6°N latitude and 169.4° to 46.9°W longitude. The cruise took place from July 30 to August 27, 2017,

142    and was segmented into five distinct phases as described in Wang et al. (2022) for detailed analysis based

143    on the ship's location, as depicted in Figure 1, and the specific sampling times and locations for each

144    phase are detailed in Table S1 and summarized as follows: Chukchi Sea section, denoted as Leg I, spans

145    from 22:00 on July 30th, 2017, to 19:00 on August 1st, 2017, covering latitudes from 66.0°N to 74.8°N

146    and longitudes from 169.4°W to 159.2°W. The high Arctic section, marked as Leg II, extends from 20:00

147    on August 10th to 5:00 on August 12th, 2017, ranging from 83.7°N to 84.6°N and from 132.0°E to

148    110.4°E. Svalbard Islands section, identified as Leg III, is from 2:00 on August 17th to 11:00 on August

149    19th, 2017, with latitudes from 82.6°N to 74.3°N and longitudes from 25.4°E to 2.1°E. Norwegian Sea

150    and Iceland section, referred to as Leg IV, occurs from 14:00 on August 23rd to 14:00 on August 25th,

151    2017, spanning from 67.0°N to 61.2°N and from 2.1°W to 25.8°W. Atlantic Ocean section, labeled as

152    Leg V, ranging from 14:00 on August 25th to 17:00 on August 27th, 2017, covers from 61.1°N to 56.2°N

153    and from 25.9°W to 46.9°W. The methodology for particle detection utilized the onboard Single Particle

154    Aerosol Mass Spectrometer (SPAMS), consistent with the techniques described by Li et al. (2011). Prior

155    to analysis, sampled particles were dried using a Nafion dryer to remove moisture. A $PM_{2.5}$ collector was

156    employed to filter out particles larger than 2.5 μm. The fine particles were then drawn into the vacuum

157    system through a critical orifice, accelerated, and focused to form a narrow particle beam. These particles

158    were subsequently exposed to two continuous Nd:YAG diode lasers (532 nm) to determine their

159    aerodynamic diameter based on their velocity. Each particle was then ionized by an Nd:YAG laser (266

160    nm) to generate positive and negative fragment ions. The ionization laser maintained a power density of

161    $1.55 \times 10^8$ W/cm^2. The resulting fragment ions were detected using a bipolar time-of-flight mass

162    spectrometer. For calibration of the SPAMS, polystyrene latex spheres (PSL Nanosphere Size Standards,

163    Duke Scientific Corp., Palo Alto) with diameters ranging from 0.2 to 2.0 μm were used. Additionally,

164    PbNO$_3$ particles with a diameter of 0.35 μm, generated by an aerosol generation and monitoring system

165    (AGM-1500, MSP Corporation, USA), were utilized for mass spectrum calibration. The sampling inlet,

166    connected to the monitoring instruments, was positioned on a mast 20 meters above the sea surface at

167    the bow of the vessel to minimize the influence of ship emissions. Sampling was conducted only while

168    the ship was in motion. A specific peak threshold was set at five units, allowing the instrument to record

169    a peak signal that surpassed this threshold, thus distinguishing it from background noise (<1 unit) in the

170    mass spectra (Zhang et al., 2021). The same instrument and samples were successfully used by Wang et

171    al. (2022) to investigate the mixing state, distribution, and photochemistry of iodine-containing particles

172    through specific identification conditions. In this study, we adopt a new perspective, focusing on black

173    carbon particles from the same samples, examining their sources, distribution, and relationships to sulfate

174    formation under distinct identification conditions, as described in detail in Section 2.2.

175    **2.2 Data processing of SPAMS data**

176        Particle size and mass spectra were analyzed using the YAADA software toolkit

177    (http://www.yaada.org/) and MATLAB (http://www.mathworks.com). Throughout the entire cruise, over

178    2,000,000 particles were sampled and sized using two continuous Nd:YAG diode lasers (532 nm). Nearly

179    290,000 particles were ionized using an Nd:YAG laser (266 nm), generating both positive and negative

180    ion mass spectrometry data during the cruise. Black carbon particles are known to produce a series of

181    characteristic signal peaks at integer multiples of 12 for the mass-to-charge ratio (m/z = ±12, ±24, ±36,

182    ±48, ±60, etc.) in the spectra (Kollner et al., 2021; Qin & Prather, 2006; Roth et al., 2016; Schmidt et al.,

183    2017; Sierau et al., 2014). Therefore, the presence of several of these signal peaks concurrently in the

184    anionic or cationic mass spectrum of a particle suggests the presence of black carbon. In this study, we

185    established specific criteria to identify black carbon particles among all ionized particles (Beddows et al.,

186    2004). A particle is determined to contain black carbon if it meets one of the following conditions:

187        (1) The signal peaks of m/z = 12, 24, and 36 appear simultaneously in the cationic mass spectrum.

188        (2) The signal peaks of m/z = -24, -36, and -48 appear simultaneously in the anionic mass spectrum.

189        Using the specified method, approximately 80,000 particles were identified as containing black

190    carbon. The average spectrum of black carbon particles is displayed in Figure S1. The figure reveals that,

191    in addition to the peak for carbon signals, there are prominent peaks for $^{39}K^+$ and $^{40}Ca^+$ in the cation

192    spectrum, as well as $^{26}CN^-$/$^{42}CNO^-$ and $^{97}HSO_4^-$ in the anion spectrum. To categorize these particles into

193 distinct groups based on the presence and intensity of ion peaks in their mass spectra, we employed the

194 Adaptive Resonance Theory neural network algorithm (ART-2a) (Song et al., 1999). The parameters set

195 for ART-2a included a vigilance factor of 0.6, a learning rate of 0.05, and a limit of 20 iterations. This

196 clustering approach is designed to include more than 95% of the total particles when used for

197 classification purposes. For the descriptive statistical analysis of the data, SPSS version 20 (IBM Inc.,

198 USA) was utilized.

199 **2.3 Satellite data acquisition**

200 In this study, the intensity of solar radiation was derived using the surface incoming shortwave flux

201 (SWGDN, in watts per square meter, W/m^2) with a 1-hour time resolution. This data was sourced from

202 the NASA Goddard Earth Sciences Data and Information Services Center (https://disc.gsfc.nasa.gov/)

203 for the specific times and locations relevant to our research.

204

205 **3    Results and Discussion**

206 **3.1  Mixing state of black carbon particles**

207 Numerous studies have established a clear link between the mixing state of black carbon particles

208 and their radiative impacts in the Arctic atmosphere. Black carbon aerosols, originating from various

209 sources, each distinctly influence their mixing states and consequently their effects on radiation. (Chung

210 & Seinfeld, 2002; Matsui et al., 2022). Utilizing the ART-2a algorithm, black carbon particles were

211 classified based on the position and intensity of characteristic peaks in their mass spectra. These particles

212 were categorized into seven main types across the entire route, as detailed in Figure 2, which includes

213 the average spectra for each type:

214    (1) **Potassium-Cyanide (K-CN):** Displayed in Figure 2a, these particles show a dominant $^{39}K^+$

215         signal in the cationic mass spectrum, with a relative peak area exceeding 0.8. Although

216         carbonaceous cations ($^{12}C^+$, $^{24}C_2^+$, $^{36}C_3^+$) are less pronounced, significant cyanide peaks ($^{42}CN^-$

217         and $^{46}CNO^-$) along with inorganic and organic carbon peaks are evident in the anionic mass

218         spectrum. Accounting for 51.8% of all black carbon particles, these strong signals suggest a

219         biomass combustion origin (Silva et al., 1999).

220    (2) **Calcium-Nitrate (Ca-NO₃):** Figure 2b shows that these particles primarily feature a strong

221         $^{40}Ca^+$ signal in the cationic mass spectrum, with a significant nitrate signal ($^{46}NO_2^-$) and

222    additional carbon peaks in the anionic mass spectrum. Comprising 23.7% of the particles, this

223    type is associated with continental dust transport, possibly from mid to low-latitude dust

224    reaching the Arctic during summer (Willis et al., 2018).

225    (3) **Potassium-Nickel-Sulfate (K-Ni-SO$_4$):** As seen in Figure 2c, these particles exhibit

226    prominent $^{39}$K$^+$ and carbonaceous cation signals in the cation mass spectrum, with notable

227    $^{59}$Ni$^+$ and intense sulfate peaks ($^{97}$HSO$_4^-$) in the anionic mass spectrum. Making up 15.9% of

228    the particles, their nickel content typically points to petroleum product combustion and other

229    anthropogenic activities (Shevchenko et al., 2003; Zhan et al., 2014).

230    (4) **Sulfate (SO$_4$):** Figure 2d illustrates these particles with strong sulfate signal peaks ($^{97}$HSO$_4^-$)

231    in the anionic mass spectrum and a significant presence of inorganic carbon cations,

232    constituting 7.6% of the total. Correlations (Figure S2a, r=0.41, p<0.01) observed between the

233    SO$_4$ and K-Ni-SO$_4$ black carbon particles indicate a common source of anthropogenic origin.

234    (5) **Potassium-Sulfate (K-SO$_4$):** Shown in Figure 2e, these particles, which account for only

235    0.6%, are characterized by strong $^{39}$K$^+$ signals in the cationic mass spectrum and sulfate peaks

236    ($^{97}$HSO$_4^-$) alongside inorganic carbon peaks in the anionic mass spectrum. Compared to SO$_4$,

237    the K-SO$_4$ and K-Ni-SO$_4$ black carbon particles exhibit a stronger correlation (Figure S2b,

238    r=0.82, p<0.01), suggesting that they also originate from similar human activities.

239    (6) **Potassium-L-Glucan (K-lev):** Figure 2f depicts these particles with $^{39}$K$^+$ and organic matter

240    signals in the cationic mass spectrum and characteristic L-glucan peaks (m/z = -45, -59, -71, -

241    73) in the anionic mass spectrum, indicative of biomass combustion and comprising 0.5% of

242    the particles (Simoneit et al., 1999).

243    Previous research has differentiated the sources of Arctic black carbon, identifying fossil fuels as

244    the primary winter source and biomass burning as the predominant summer source, with an annual

245    average biomass combustion contribution of 39±10% to atmospheric black carbon (Winiger et al., 2019).

246    Further studies have shown that biomass combustion contributes over 90% to Arctic ice and snow black

247    carbon (Hegg et al., 2009). This study's cluster analysis quantitatively estimated that biomass combustion

248    is the main summer source, accounting for 52.3% of black carbon aerosols, with specific mixed types

249    including K-CN and K-lev. Anthropogenic and transported sources from mid and low latitudes account

250    for 24.0% and 23.7%, respectively, with specific mixed types including K-Ni-SO$_4$, SO$_4$, K-SO$_4$, and Ca-

251     $NO_3$.

252     **3.2 Spatial distribution of black carbon particles**

253          As illustrated in Figure S3, the hourly concentration of black carbon particles along the surveyed

254     route varied substantially, ranging from 0 to 3000 particles per hour. In the initial three segments, the

255     concentration remained relatively low, with the highest value not surpassing 1500 particles per hour.

256     Conversely, in Leg IV, the concentration of black carbon particles was markedly higher, reaching a peak

257     near 3000/h, and Leg V also recorded a significant concentration of 2500/h. The proportion of black

258     carbon particles varied from 0% to 60% across the route. Unlike the number concentration, the

259     distribution of the proportion of black carbon particles was more uniform throughout the voyage. Figure

260     3 displays the hourly number and proportion of black carbon particles by box plots. The mean

261     concentrations of black carbon particles in Legs I-V were 198/h, 148/h, 255/h, 757/h, and 345/h,

262     respectively. The corresponding average proportions were 19.8 (±10.7) %, 24.4 (±16.2) %, 26.6

263     (±13.6) %, 26.1 (±10.9) %, and 26.5 (±10.5) %. Although the average concentration of black carbon

264     particles varied significantly among the different segments, the proportion of black carbon particles

265     relative to all particles remained relatively consistent, particularly in the last three segments where the

266     average proportion showed minimal variation. This consistency suggests that black carbon particles are

267     prevalent in the Arctic summer ocean boundary layer and constitute a significant and uniformly

268     distributed component of the atmospheric aerosol. The overall average proportion of black carbon

269     particles for all segments was 24.7 (±13.6) %.

270          While the average proportion of black carbon particles remained relatively consistent across

271     different segments, spatial variations in the proportions of black carbon particle types were observed

272     (Figure 4), suggesting diverse sources of black carbon aerosols in different regions. In Leg I, the

273     predominant black carbon types were Ca-$NO_3$, which accounted for about 50% of the particles, followed

274     by K-CN at approximately 25%, and K-Ni-$SO_4$ and $SO_4$ each at about 10%. K-$SO_4$ and K-lev were nearly

275     absent. In Leg II, K-CN was the most significant, comprising about 70% of particles, with Ca-$NO_3$ at

276     around 15%, K-Ni-$SO_4$ and K-lev each at about 5%, $SO_4$ less than 5%, and K-$SO_4$ almost nonexistent.

277     Leg III saw a dominance of K-CN and Ca-$NO_3$, each making up about 50%, with other types collectively

278     less than 5%. Leg IV featured K-CN as the most prevalent, at about 60%, with K-Ni-$SO_4$ and Ca-$NO_3$

279     each contributing around 20%, $SO_4$ at about 5%, and negligible amounts of K-$SO_4$ and K-lev. Leg V had

280    a similar composition to Leg IV, but with a reduced proportion of Ca-NO$_3$ at about 10% and an increased

281    proportion of SO$_4$ to about 15%. The distribution of mixed types of black carbon particles helped to

282    elucidate the source contributions in different regions. In the central Arctic Ocean, the Norwegian Sea-

283    Iceland, and the North Atlantic Ocean, biomass combustion was the primary source of black carbon,

284    accounting for more than 50% of particles, particularly in the central Arctic Ocean where it exceeded

285    70%. In the Chukchi Sea region, terrestrial transport from mid and low latitudes was the dominant source,

286    also accounting for more than 50% of particles, with biomass combustion and anthropogenic pollution

287    sources each contributing about 25%. Near Svalbard, biomass combustion sources and terrestrial

288    transport were the main contributors and were roughly equal in proportion. Previous studies have

289    indicated that black carbon aerosols from different sources possess varying thicknesses of coatings,

290    thereby affecting their radiative impacts differently (Matsui et al., 2022). In our study, the sources of

291    black carbon aerosols in different regions were quantitatively estimated, which is crucial for a more

292    accurate assessment of the climate effects of Arctic black carbon aerosols.

293    **3.3 Photochemical processes of Arctic black carbon aerosols**

294    In urban environments, it has been established that black carbon particles are photoactive, capable

295    of releasing reactive oxygen species such as excited oxygen molecules ($^1O_2$) and hydroxyl radicals. These

296    species participate in atmospheric chemical processes, including the catalytic formation of sulfate

297    (Gehling & Dellinger, 2013; Li et al., 2018; Li et al., 2019; Zhang et al., 2020; Zhang et al., 2021). In the

298    Arctic Ocean boundary layer, the release of dimethyl sulfur by marine organisms and its subsequent

299    oxidation to sulfate is known to have significant environmental and climatic impacts (Bates et al., 1987;

300    Charlson et al., 1987; Rap et al., 2013). However, the potential role of black carbon particles in enhancing

301    this sulfate formation process remains unclear, a topic we explore in this section. Although black carbon

302    particles facilitate the catalysis of sulfate formation, they do not appear to significantly promote nitrate

303    formation (Zhang et al., 2021). Consequently, this leads to a relative enrichment of sulfate compared to

304    nitrate in particles containing black carbon, increasing the sulfate to nitrate mass concentration ratio

305    (SNR). In this study, we utilized the ratio of the relative peak areas of sulfate ($^{97}HSO_4^-$) to nitrate ($^{46}NO_2^-$)

306    to describe SNR, specifically denote the relative enrichment of sulfate in black carbon particles. The

307    SNR for black carbon particles varied widely, ranging from 0 to 1000, with an average value of 32.25

308    and a median value of 8.14. This contrasts with measurements from a previous single-particle study of

309  urban black carbon during summer, which reported SNR values ranging from 0 to 5 and a median value

310  of about 2 (Zhang et al., 2021). The notably higher SNR in the Arctic summer suggests that emissions of

311  sulfur-containing gases by marine organisms in the ocean boundary layer may provide a substantial

312  number of precursors for sulfate generation. Additionally, we calculated the SNR for the most common

313  sea salt particles in the ocean boundary layer, which ranged from 0 to 6, with an average of 0.34 and a

314  median of 0.15. This comparison shows that the SNR of black carbon particles is significantly higher

315  than that of sea salt particles, indicating substantial sulfate enrichment in black carbon particles.

316  Moreover, we used the cumulative relative peak area values ($R_{BC}$) of inorganic carbonaceous anions ($^{12}C^{+}$,

317  $^{24}C^{\pm}$, $^{36}C^{\pm}$, $^{48}C^{-}$) in black carbon-containing particles to indicate the content of black carbon components

318  within the particles. As illustrated in Figure 5, the SNR value increased with the rising content of black

319  carbon, displaying a moderate correlation (r = 0.37, p < 0.01). This trend suggests that higher black

320  carbon content in particles tends to enhance sulfate enrichment over nitrate, indicating that black carbon

321  components can promote sulfate formation in the Arctic region.

322      The observed phenomenon of elevated SNR in black carbon particles can be attributed to several

323  factors: (1) Common Source for Black Carbon and Sulfate Precursors: Black carbon and sulfate, along

324  with their precursors, possibly share common sources, contributing to the increased SNR in black carbon

325  particles. Predominantly, black carbon aerosols originate from biomass combustion, which accounts for

326  over half of these emissions, supplemented by anthropogenic sources and transport from mid to low

327  latitudes in this study. In the ocean boundary layer, sulfur-containing gases emitted by marine biogenic

328  sources are primary precursors for sulfate (Becagli et al., 2016; Gondwe et al., 2003; Jarnikova et al.,

329  2018). However, anthropogenic black carbon aerosols, such as those from ship-based emissions, may

330  also emit significant amounts of $SO_2$ (Davis et al., 2001; Krause et al., 2021; Winther et al., 2014). After

331  excluding these anthropogenic sources, the average SNR for black carbon particles from biomass

332  combustion sources was calculated at 7.85, significantly higher than in sea salt particles. Although higher

333  $SO_2$ concentrations are noted in biomass combustion air masses, an increase in nitrogen oxides (Leino et

334  al., 2014) suggests a limited impact on the SNR; (2) Catalysis by Transition Metal Elements: Transition

335  metals such as iron and vanadium found in black carbon particles can catalyze the formation of sulfate

336  (Ault et al., 2010; Zhang et al., 2019). These metals typically originate from anthropogenic activities,

337  including ship-based emissions, and are consequently enriched in anthropogenic black carbon aerosols.

338 As the concentration of black carbon in the particles increases, so too does the concentration of these

339 catalytic metals, enhancing their effect on sulfate formation. Despite this, even after accounting for

340 sources that might skew data, such as those rich in transition metals, black carbon particles still exhibit

341 a higher enrichment of sulfate compared to sea salt particles. After ruling out these factors, it is evident

342 that black carbon itself contributes to the enhancement of sulfate formation, aligning with observations

343 in urban environments (Zhang et al., 2021). To further explore the potential involvement of

344 photochemical processes in this enhancement, black carbon particles were categorized based on varying

345 levels of sunlight intensity. The SWGDN served as an indicator of sunlight intensity changes. Black

346 carbon particles were segmented into five groups based on their SWGDN values, spanning from 0-100,

347 100-200, 200-300, 300-400, and over 400 W/m^2. As depicted in Figure 6, the SNR values are lower

348 when the SWGDN value is below 200 W/m^2. However, as the SWGDN value increases, there is a

349 corresponding rise in SNR values. The average SNR values for black carbon particles across these groups

350 were 25.2, 21.4, 44.3, 63.1, and 174.4, respectively. These findings underscore a significant impact of

351 sunlight intensity on the concentration of sulfate in black carbon particles, suggesting that light-driven

352 photochemical reactions may play a crucial role in this process.

353 The formation of sulfate and nitrate is intrinsically linked to the presence of oxidizing agents such

354 as hydroxyl radicals and active halogens, which are often involved in photochemical processes (Chen et

355 al., 2017; Liu et al., 2021; Shao et al., 2019). Additionally, conditions of strong light are thought to

356 facilitate the degradation of nitrate, potentially leading to an increased SNR in black carbon particles

357 (Zhang et al., 2021). These factors may significantly contribute to the observed light intensity-dependent

358 enrichment of sulfate in black carbon particles. To evaluate this possibility, the SNR values of sea salt

359 particles under varying lighting conditions, as shown in Figure 6, do not mirror the changes observed in

360 black carbon particles. The average SNR values for sea salt particles across the five groups—ranging

361 from low to high sunlight intensities—were 0.33, 0.28, 0.53, 0.52, and 0.33, respectively. Notably, while

362 there is a slight increase in SNR values for sea salt particles within the 200-400 W/m² range of SWGDN,

363 the values decrease again when SWGDN exceeds 400 W/m², aligning with the lower values observed

364 under less intense light conditions. This disparity suggests that while sunlight intensity influences the

365 photoactivity of black carbon, leading to the release of reactive oxygen species and subsequent sulfate

366 formation, it does not significantly impact the SNR in sea salt particles. This indicates a unique

367   photochemical sensitivity in black carbon particles that enhances sulfate formation under higher sunlight

368   conditions—a process consistent with photochemistry observed in urban environments, rather than being

369   caused by degradation of nitrate (Zhang et al., 2020; Zhang et al., 2021). Furthermore, the interaction of

370   sulfate and organic carbon with black carbon aerosols can significantly alter the optical properties of

371   these particles, thereby increasing their positive radiative forcing (Chung & Seinfeld, 2002). This

372   photochemical facilitation not only affects the chemical composition of the aerosols but also their

373   radiative properties, which could have profound implications for the Arctic climate. Such interactions

374   and their climatic effects underscore the importance of incorporating this photochemistry into future

375   climate models to accurately predict and mitigate the impacts of black carbon in polar regions.

376

377   **4    Summary and Implications**

378   In this research, we focused on extracting and analyzing black carbon-containing particles from

379   collected atmospheric samples to understand their mixing states, sources, spatial distribution variations,

380   and their role in enhancing sulfate formation through photochemical processes. The black carbon

381   particles were categorized into six distinct groups based on their mixing states: K-CN, Ca-NO$_3$, K-Ni-

382   SO$_4$, SO$_4$, K-SO$_4$, and K-lev. Our findings indicate that K-CN and K-lev, which are primarily products

383   of biomass combustion, represent 52.3% of the sampled particles. Ca-NO$_3$, linked to terrestrial sources,

384   accounted for 23.7% of the particles. The remaining categories—K-Ni-SO$_4$, SO$_4$, and K-SO$_4$—are

385   predominantly derived from anthropogenic activities, such as emissions from ships, contributing to 24.0%

386   of the particles. Spatial analysis revealed that the distribution of black carbon-containing particles is

387   relatively stable across the Arctic regions, suggesting their pervasive presence in the Arctic summer

388   ocean boundary layer as a significant component of atmospheric aerosols. However, the source

389   contributions of these particles vary spatially. In the central Arctic Ocean and areas near the Norwegian

390   Sea-Iceland and the North Atlantic Ocean, more than 50% of the black carbon particles originate from

391   biomass combustion, with the figure rising above 70% in the central Arctic Ocean. In contrast, in the

392   Chukchi Sea region, terrestrial transport from middle and low latitudes is the dominant source,

393   accounting for more than 50% of the black carbon particles, while biomass combustion and

394   anthropogenic pollution each contribute approximately 25%. Near Svalbard, biomass combustion

395   sources and terrestrial transport are equally significant contributors to the presence of black carbon

396 particles. Moreover, our study confirms that black carbon particles in the Arctic Ocean boundary layer

397 significantly enhance sulfate formation through their involvement in photochemical reactions. This

398 interaction not only alters the mixing state of the black carbon aerosols but also affects their radiative

399 properties, potentially influencing the climate. This underscores the importance of understanding the

400 complex photochemistry of black carbon in Arctic aerosols for future climate modeling and assessment

401 strategies.

402

406

407 **Data availability**

408     Access to the raw data and products is available at DOI:10.5281/zenodo.13883324 or by contacting

409 either the corresponding author, Zhouqing Xie, at zqxie@ustc.edu.cn, or the first author, Longquan Wang,

410 at wlq1995@mail.ustc.edu.cn. The SWGDN data featured in this publication can be accessed publicly

411 through the NASA Goddard Earth Sciences Data and Information Services Center at

412 https://disc.gsfc.nasa.gov/.

413

414 **Declaration of competing interests**

415     The authors declare that they have no known competing financial interests or personal relationships

416 that cloud have appeared to influence the work reported in this paper.

417    **Author contribution:**

418    Conceptualization: Zhouqing Xie

419    Data curation: Longquan Wang, Jinpei Yan

420    Investigation: Longquan Wang, Jinpei Yan

421    Formal analysis: Longquan Wang, Afeng Chen, Bei Jiang, Fange Yue, Xiawei Yu, Zhouqing Xie

422    Visualization: Longquan Wang

423    Funding acquisition: Zhouqing Xie

424    Supervision: Zhouqing Xie

425    Writing – original draft: Longquan Wang

426    Writing – review & editing: Longquan Wang, Zhouqing Xie

427   **Reference**

428   Ault, A. P., Gaston, C. J., Wang, Y., Dominguez, G., Thiemens, M. H., & Prather, K. A.（2010）.

429       Characterization of the Single Particle Mixing State of Individual Ship Plume Events Measured

430       at the Port of Los Angeles. *Environmental Science & Technology, 44*（6）, 1954-1961.

431       doi:10.1021/es902985h

432   Bates, T. S., Charlson, R. J., & Gammon, R. H.（1987）. EVIDENCE FOR THE CLIMATIC ROLE

433       OF MARINE BIOGENIC SULFUR. *Nature, 329*（6137）, 319-321. doi:10.1038/329319a0

434   Becagli, S., Lazzara, L., Marchese, C., Dayan, U., Ascanius, S. E., Cacciani, M., . . . Udisti, R.（2016）.

435       Relationships linking primary production, sea ice melting, and biogenic aerosol in the Arctic.

436       *Atmospheric Environment, 136*, 1-15. doi:10.1016/j.atmosenv.2016.04.002

437   Beddows, D. C., Donovan, R. J., Harrison, R. M., Heal, M. R., Kinnersley, R. P., King, M. D., . . .

438       Thompson, K. C.（2004）. Correlations in the chemical composition of rural background

439       atmospheric aerosol in the UK determined in real time using time-of-flight mass spectrometry.

440       *J Environ Monit, 6*（2）, 124-133. doi:10.1039/b311209h

441   Bond, T. C., & Bergstrom, R. W.（2006）. Light absorption by carbonaceous particles: An investigative

442       review. *Aerosol Science and Technology, 40*（1）, 27-67. doi:10.1080/02786820500421521

443   Charlson, R. J., Lovelock, J. E., Andreae, M. O., & Warren, S. G.（1987）. OCEANIC

444       PHYTOPLANKTON, ATMOSPHERIC SULFUR, CLOUD ALBEDO AND CLIMATE.

445       *Nature, 326*（6114）, 655-661. doi:10.1038/326655a0

446   Chen, Q., Schmidt, J. A., Shah, V., Jaeglé, L., Sherwen, T., & Alexander, B.（2017）. Sulfate production

447       by reactive bromine: Implications for the global sulfur and reactive bromine budgets.

448       *Geophysical Research Letters, 44*（13）, 7069-7078. doi:10.1002/2017gl073812

449   Ching, J., Riemer, N., & West, M.（2012）. Impacts of black carbon mixing state on black carbon

450       nucleation scavenging: Insights from a particle-resolved model. *Journal of Geophysical*

451       *Research-Atmospheres, 117*. doi:10.1029/2012jd018269

452   Ching, J., West, M., & Riemer, N.（2018）. Quantifying Impacts of Aerosol Mixing State on Nucleation-

453       Scavenging of Black Carbon Aerosol Particles. *Atmosphere, 9*（1）. doi:10.3390/atmos9010017

454   Chung, S. H., & Seinfeld, J. H.（2002）. Global distribution and climate forcing of carbonaceous aerosols.

455       *Journal of Geophysical Research-Atmospheres, 107*（D19）. doi:10.1029/2001jd001397

456 Clarke, A. D., & Noone, K. J.　(1985)．SOOT IN THE ARCTIC SNOWPACK - A CAUSE FOR

457   PERTURBATIONS IN RADIATIVE-TRANSFER. *Atmospheric Environment, 19*（12），2045-

458   2053. doi:10.1016/0004-6981（85）90113-1

459 Davis, D. D., Grodzinsky, G., Kasibhatla, P., Crawford, J., Chen, G., Liu, S., . . . Sandholm, S.　(2001)．

460   Impact of ship emissions on marine boundary layer NOx and SO2 distributions over the Pacific

461   basin. *Geophysical Research Letters, 28*（2），235-238. doi:10.1029/2000gl012013

462 Dou, T.-F., & Xiao, C.-D.　(2016)．An overview of black carbon deposition and its radiative forcing

463   over the Arctic. *Advances in Climate Change Research, 7*（3），115-122.

464   doi:10.1016/j.accre.2016.10.003

465 Eleftheriadis, K., Vratolis, S., & Nyeki, S.　(2009)．Aerosol black carbon in the European Arctic:

466   Measurements at Zeppelin station, Ny-Alesund, Svalbard from 1998-2007. *Geophysical*

467   *Research Letters, 36*. doi:10.1029/2008gl035741

468 Evangeliou, N., Balkanski, Y., Hao, W. M., Petkov, A., Silverstein, R. P., Corley, R., . . . Skov, H.　(2016)．

469   Wildfires in northern Eurasia affect the budget of black carbon in the Arctic - a 12-year

470   retrospective synopsis　(2002-2013)．*Atmospheric Chemistry and Physics, 16*（12），7587-

471   7604. doi:10.5194/acp-16-7587-2016

472 Flanner, M. G., Zender, C. S., Randerson, J. T., & Rasch, P. J.　(2007)．Present-day climate forcing and

473   response from black carbon in snow. *Journal of Geophysical Research-Atmospheres, 112*（D11）.

474   doi:10.1029/2006jd008003

475 Gehling, W., & Dellinger, B.　(2013)．Environmentally Persistent Free Radicals and Their Lifetimes

476   in PM2.5. *Environmental Science & Technology, 47*（15），8172-8178. doi:10.1021/es401767m

477 Gondwe, M., Krol, M., Gieskes, W., Klaassen, W., & de Baar, H.　(2003)．The contribution of ocean-

478   leaving DMS to the global atmospheric burdens of DMS, MSA, SO2, and NSS SO4=. *Global*

479   *Biogeochemical Cycles, 17*（2）. doi:10.1029/2002gb001937

480 Hansen, J., Sato, M., Ruedy, R., Nazarenko, L., Lacis, A., Schmidt, G. A., . . . Zhang, S.　(2005)．

481   Efficacy of climate forcings. *Journal of Geophysical Research-Atmospheres, 110*（D18）.

482   doi:10.1029/2005jd005776

483 Hegg, D. A., Warren, S. G., Grenfell, T. C., Doherty, S. J., Larson, T. V., & Clarke, A. D.　(2009)．

484   Source Attribution of Black Carbon in Arctic Snow. *Environmental Science & Technology, 43*

485  (11), 4016-4021. doi:10.1021/es803623f

486  Jacobson, M. Z. (2001). Strong radiative heating due to the mixing state of black carbon in atmospheric

487  aerosols. *Nature, 409* (6821), 695-697. doi:10.1038/35055518

488  Jarnikova, T., Dacey, J., Lizotte, M., Levasseur, M., & Tortell, P. (2018). The distribution of methylated

489  sulfur compounds, DMS and DMSP, in Canadian subarctic and Arctic marine waters during

490  summer 2015. *Biogeosciences, 15* (8), 2449-2465. doi:10.5194/bg-15-2449-2018

491  Kollner, F., Schneider, J., Willis, M. D., Schulz, H., Kunkel, D., Bozem, H., . . . Borrmann, S. (2021).

492  Chemical composition and source attribution of sub-micrometre aerosol particles in the

493  summertime Arctic lower troposphere. *Atmospheric Chemistry and Physics, 21* (8), 6509-6539.

494  doi:10.5194/acp-21-6509-2021

495  Krause, K., Wittrock, F., Richter, A., Schmitt, S., Pohler, D., Weigelt, A., & Burrows, J. P. (2021).

496  Estimation of ship emission rates at a major shipping lane by long-path DOAS measurements.

497  *Atmospheric Measurement Techniques, 14* (8), 5791-5807. doi:10.5194/amt-14-5791-2021

498  Leino, K., Riuttanen, L., Nieminen, T., Dal Maso, M., Vaananen, R., Pohja, T., . . . Kulmala, M. (2014).

499  Biomass-burning smoke episodes in Finland from eastern European wildfires. *Boreal*

500  *Environment Research, 19*, 275-292.

501  Li, L., Huang, Z. X., Dong, J. G., Li, M., Gao, W., Nian, H. Q., . . . Zhou, Z. (2011). Real time bipolar

502  time-of-flight mass spectrometer for analyzing single aerosol particles. *International Journal of*

503  *Mass Spectrometry, 303* (2-3), 118-124. doi:10.1016/j.ijms.2011.01.017

504  Li, M., Bao, F. X., Zhang, Y., Sheng, H., Chen, C. C., & Zhao, J. C. (2019). Photochemical Aging of

505  Soot in the Aqueous Phase: Release of Dissolved Black Carbon and the Formation of O-1 (2).

506  *Environmental Science & Technology, 53* (21), 12311-12319. doi:10.1021/acs.est.9b02773

507  Li, M., Bao, F. X., Zhang, Y., Song, W. J., Chen, C. C., & Zhao, J. C. (2018). Role of elemental carbon

508  in the photochemical aging of soot. *Proceedings of the National Academy of Sciences of the*

509  *United States of America, 115* (30), 7717-7722. doi:10.1073/pnas.1804481115

510  Liu, T. Y., Chan, A. W. H., & Abbatt, J. P. D. (2021). Multiphase Oxidation of Sulfur Dioxide in

511  Aerosol Particles: Implications for Sulfate Formation in Polluted Environments. *Environmental*

512  *Science & Technology, 55* (8), 4227-4242. doi:10.1021/acs.est.0c06496

513  Matsui, H., Mori, T., Ohata, S., Moteki, N., Oshima, N., Goto-Azuma, K., . . . Kondo, Y. (2022).

514    Contrasting source contributions of Arctic black carbon to atmospheric concentrations,

515    deposition flux, and atmospheric and snow radiative effects. *Atmospheric Chemistry and*

516    *Physics, 22* （13）, 8989-9009. doi:10.5194/acp-22-8989-2022

517  Qi, L., Li, Q. B., Li, Y. R., & He, C. L. （2017）. Factors controlling black carbon distribution in the

518    Arctic. *Atmospheric Chemistry and Physics, 17* （2）, 1037-1059. doi:10.5194/acp-17-1037-

519    2017

520  Qin, X. Y., & Prather, K. A. （2006）. Impact of biomass emissions on particle chemistry during the

521    California Regional Particulate Air Quality Study. *International Journal of Mass Spectrometry,*

522    *258* （1-3）, 142-150. doi:10.1016/j.ijms.2006.09.004

523  Quinn, P. K., Shaw, G., Andrews, E., Dutton, E. G., Ruoho-Airola, T., & Gong, S. L. （2007）. Arctic

524    haze: current trends and knowledge gaps. *Tellus Series B-Chemical and Physical Meteorology,*

525    *59* （1）, 99-114. doi:10.1111/j.1600-0889.2006.00236.x

526  Ramanathan, V., & Carmichael, G. （2008）. Global and regional climate changes due to black carbon.

527    *Nature Geoscience, 1* （4）, 221-227. doi:10.1038/ngeo156

528  Rap, A., Scott, C. E., Spracklen, D. V., Bellouin, N., Forster, P. M., Carslaw, K. S., . . . Mann, G. （2013）.

529    Natural aerosol direct and indirect radiative effects. *Geophysical Research Letters, 40* （12）,

530    3297-3301. doi:10.1002/grl.50441

531  Roth, A., Schneider, J., Klimach, T., Mertes, S., van Pinxteren, D., Herrmann, H., & Borrmann, S.

532    （2016）. Aerosol properties, source identification, and cloud processing in orographic clouds

533    measured by single particle mass spectrometry on a central European mountain site during

534    HCCT-2010. *Atmospheric Chemistry and Physics, 16* （2）, 505-524. doi:10.5194/acp-16-505-

535    2016

536  Schmidt, S., Schneider, J., Klimach, T., Mertes, S., Schenk, L. P., Kupiszewski, P., . . . Borrmann, S.

537    （2017）. Online single particle analysis of ice particle residuals from mountain-top mixed-

538    phase clouds using laboratory derived particle type assignment. *Atmospheric Chemistry and*

539    *Physics, 17* （1）, 575-594. doi:10.5194/acp-17-575-2017

540  Serreze, M. C., & Barry, R. G. （2011）. Processes and impacts of Arctic amplification: A research

541    synthesis. *Global and Planetary Change, 77* （1-2）, 85-96. doi:10.1016/j.gloplacha.2011.03.004

542  Shao, J., Chen, Q., Wang, Y., Lu, X., He, P., Sun, Y., . . . Alexander, B. （2019）. Heterogeneous sulfate

543    aerosol formation mechanisms during wintertime Chinese haze events: air quality model

544    assessment using observations of sulfate oxygen isotopes in Beijing. *Atmospheric Chemistry*

545    *and Physics, 19*（9）, 6107-6123. doi:10.5194/acp-19-6107-2019

546   Sharma, S., Andrews, E., Barrie, L. A., Ogren, J. A., & Lavoue, D.    （2006）. Variations and sources of

547    the equivalent black carbon in the high Arctic revealed by long-term observations at Alert and

548    Barrow: 1989-2003. *Journal of Geophysical Research-Atmospheres, 111*（D14）.

549    doi:10.1029/2005jd006581

550   Sharma, S., Barrie, L. A., Magnusson, E., Brattstrom, G., Leaitch, W. R., Steffen, A., & Landsberger, S.

551    （2019）. A Factor and Trends Analysis of Multidecadal Lower Tropospheric Observations of

552    Arctic Aerosol Composition, Black Carbon, Ozone, and Mercury at Alert, Canada. *Journal of*

553    *Geophysical Research-Atmospheres, 124*（24）, 14133-14161. doi:10.1029/2019jd030844

554   Sharma, S., Lavoue, D., Cachier, H., Barrie, L. A., & Gong, S. L.    （2004）. Long-term trends of the

555    black carbon concentrations in the Canadian Arctic. *Journal of Geophysical Research-*

556    *Atmospheres, 109*（D15）. doi:10.1029/2003jd004331

557   Shevchenko, V., Lisitzin, A., Vinogradova, A., & Stein, R.    （2003）. Heavy metals in aerosols over the

558    seas of the Russian Arctic. *Science of the Total Environment, 306*（1-3）, 11-25.

559    doi:10.1016/s0048-9697（02）00481-3

560   Sierau, B., Chang, R. Y. W., Leck, C., Paatero, J., & Lohmann, U.    （2014）. Single-particle

561    characterization of the high-Arctic summertime aerosol. *Atmospheric Chemistry and Physics,*

562    *14*（14）, 7409-7430. doi:10.5194/acp-14-7409-2014

563   Silva, P. J., Liu, D. Y., Noble, C. A., & Prather, K. A.    （1999）. Size and chemical characterization of

564    individual particles resulting from biomass burning of local Southern California species.

565    *Environmental Science & Technology, 33*（18）, 3068-3076. doi:10.1021/es980544p

566   Simoneit, B. R. T., Schauer, J. J., Nolte, C. G., Oros, D. R., Elias, V. O., Fraser, M. P., . . . Cass, G. R.

567    （1999）. Levoglucosan, a tracer for cellulose in biomass burning and atmospheric particles.

568    *Atmospheric Environment, 33*（2）, 173-182. doi:10.1016/s1352-2310（98）00145-9

569   Song, X. H., Hopke, P. K., Fergenson, D. P., & Prather, K. A.    （1999）. Classification of single particles

570    analyzed by ATOFMS using an artificial neural network, ART-2A. *Analytical Chemistry, 71*（4）,

571    860-865. doi:10.1021/ac9809682

572    Wang, H. L., Rasch, P. J., Easter, R. C., Singh, B., Zhang, R. D., Ma, P. L., . . . Beagley, N.    （2014）.

573        Using an explicit emission tagging method in global modeling of source-receptor relationships

574        for black carbon in the Arctic: Variations, sources, and transport pathways. *Journal of*

575        *Geophysical Research-Atmospheres, 119* （22）, 12888-12909. doi:10.1002/2014jd022297

576    Wang, L., Yan, J., Saiz-Lopez, A., Jiang, B., Yue, F., Yu, X., & Xie, Z.    （2022）. Mixing state and

577        distribution of iodine-containing particles in Arctic Ocean during summertime. *Science of the*

578        *Total Environment, 834*. doi:10.1016/j.scitotenv.2022.155030

579    Willis, M. D., Leaitch, W. R., & Abbatt, J. P. D.    （2018）. Processes Controlling the Composition and

580        Abundance of Arctic Aerosol. *Reviews of Geophysics, 56* （4）, 621-671.

581        doi:10.1029/2018rg000602

582    Winiger, P., Barrett, T. E., Sheesley, R. J., Huang, L., Sharma, S., Barrie, L. A., . . . Gustafsson, O.  （2019）.

583        Source apportionment of circum-Arctic atmospheric black carbon from isotopes and modeling.

584        *Science Advances, 5* （2）. doi:10.1126/sciadv.aau8052

585    Winther, M., Christensen, J. H., Plejdrup, M. S., Ravn, E. S., Eriksson, O. F., & Kristensen, H. O.  （2014）.

586        Emission inventories for ships in the arctic based on satellite sampled AIS data. *Atmospheric*

587        *Environment, 91*, 1-14. doi:10.1016/j.atmosenv.2014.03.006

588    Zhang, F., Wang, Y., Peng, J. F., Chen, L., Sun, Y. L., Duan, L., . . . Zhang, R. Y.    （2020）. An unexpected

589        catalyst dominates formation and radiative forcing of regional haze. *Proceedings of the National*

590        *Academy of Sciences of the United States of America, 117* （8）, 3960-3966.

591        doi:10.1073/pnas.1919343117

592    Zhang, G. H., Fu, Y. Z., Peng, X. C., Sun, W., Shi, Z. B., Song, W., . . . Bi, X. H.    （2021）. Black Carbon

593        Involved Photochemistry Enhances the Formation of Sulfate in the Ambient Atmosphere:

594        Evidence From In Situ Individual Particle Investigation. *Journal of Geophysical Research-*

595        *Atmospheres, 126* （19）. doi:10.1029/2021jd035226

596    Zhan, J. Q., Gao, Y., Li, W., Chen, L. Q., Lin, H. M., & Lin, Q.    （2014）. Effects of ship emissions on

597        summertime aerosols at Ny-Alesund in the Arctic. *Atmospheric Pollution Research, 5* （3）,

598        500-510. doi:10.5094/apr.2014.059

599 **Figure Captions**

600 **Figure 1.** Sampling locations from open water to the high Arctic are indicated by a blue line. The

601 expedition is divided into five segments, each outlined by dashed red boxes: Chukchi Sea section,

602 denoted as Leg I, spans from 22:00 on July 30th, 2017, to 19:00 on August 1st, 2017, covering latitudes

603 from 66.0°N to 74.8°N and longitudes from 169.4°W to 159.2°W. The high Arctic section, marked as

604 Leg II, extends from 20:00 on August 10th to 5:00 on August 12th, 2017, ranging from 83.7°N to 84.6°N

605 and from 132.0°E to 110.4°E. Svalbard Islands section, identified as Leg III, is from 2:00 on August 17th

606 to 11:00 on August 19th, 2017, with latitudes from 82.6°N to 74.3°N and longitudes from 25.4°E to 2.1°E.

607 Norwegian Sea and Iceland section, referred to as Leg IV, occurs from 14:00 on August 23rd to 14:00 on

608 August 25th, 2017, spanning from 67.0°N to 61.2°N and from 2.1°W to 25.8°W. Atlantic Ocean section,

609 labeled as Leg V, spanning from 14:00 on August 25th to 17:00 on August 27th, 2017, covers from

610 61.1°N to 56.2°N and from 25.9°W to 46.9°W.

611 **Figure 2.** Spectra of various types of black carbon particles with peaks displaying strong signals

612 highlighted in blue. The X-axis represents the mass-to-charge ratio (m/z), and the Y-axis shows the

613 relative peak area. The cation spectrum is presented in the upper half of each map, while the anion

614 spectrum is depicted in the lower half. (a) Spectra of K-CN black carbon particles; (b) Spectra of Ca-

615 $NO_3$ black carbon particles; (c) Spectra of K-Ni-$SO_4$ black carbon particles; (d) Spectra of $SO_4$ black

616 carbon particles; (e) Spectra of K-$SO_4$ black carbon particles; (f) Spectra of K-lev black carbon particles.
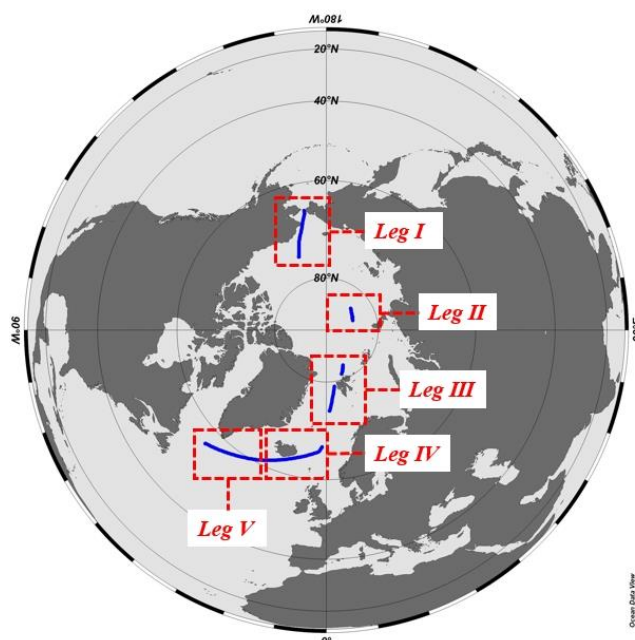
617 **Figure 3.** Box plots of hourly counts (in red) and fractions (in blue) of black carbon particles from Leg

618 I to Leg V. The tops and bottoms of the boxes indicate the upper and lower quartile values, respectively.

619 Horizontal lines within the boxes denote median values. Hollow squares and dotted black lines represent

620 mean values. Vertical whiskers extend to scattered values above and below the boxes, with caps on the

621 whiskers indicating maximum and minimum values. Cross symbols mark the 99th and 1st percentile

622 values, respectively.

623 **Figure 4.** Fraction of each type of black carbon particles from Leg I to Leg V. Different colors represent

624 various types of black carbon particles: blue for K-CN, green for Ca-$NO_3$, orange for K-Ni-$SO_4$, magenta

625 for $SO_4$, cyan for K-$SO_4$, and red for K-lev.

626 **Figure 5.** Correlation of SNR and $R_{BC}$ in black carbon particles. A red dashed line indicates the linear fit

627 curve, with the correlation coefficient (r) and significance level (p) provided.
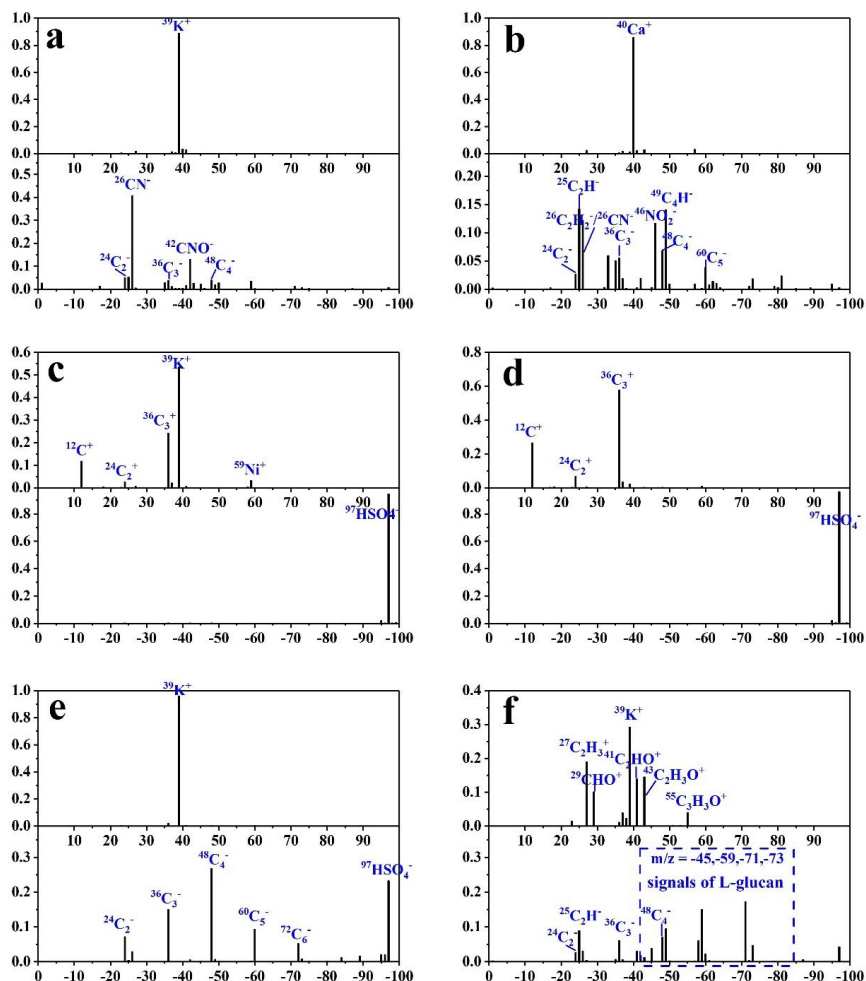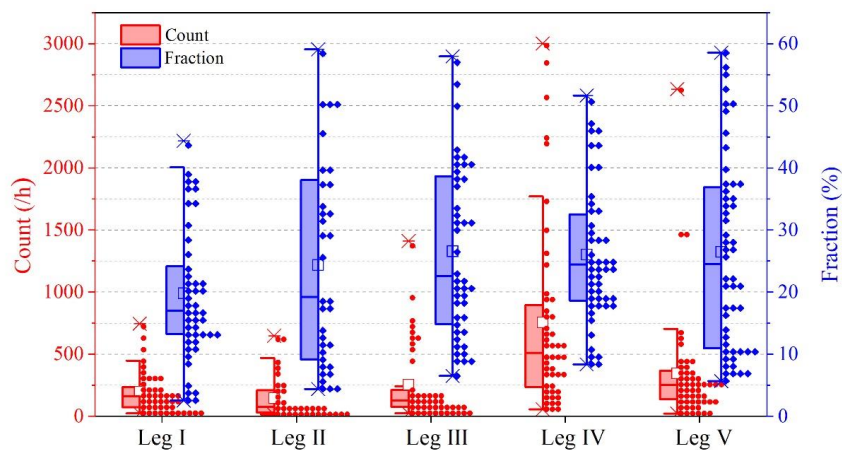
628   **Figure 6**. Box plots of SNR for sea salt particles (in red) and black carbon particles (in blue), grouped

629   by SWGDN. The upper and lower parts of the boxes indicate the quartile values, while the horizontal

630   lines within the boxes denote the median values. Hollow squares and black dotted lines show the mean

631   values. Vertical whiskers extend to capture scattered values above and below the boxes, with caps on the

632   whiskers indicating the maximum and minimum values. Cross symbols mark the 99th and 1st percentile

633   values, respectively.

**Figure 1.** Sampling locations from open water to the high Arctic are indicated by a blue line. The expedition is divided into five segments, each outlined by dashed red boxes: Chukchi Sea section, denoted as Leg I, spans from 22:00 on July 30th, 2017, to 19:00 on August 1st, 2017, covering latitudes from 66.0°N to 74.8°N and longitudes from 169.4°W to 159.2°W. The high Arctic section, marked as Leg II, extends from 20:00 on August 10th to 5:00 on August 12th, 2017, ranging from 83.7°N to 84.6°N and from 132.0°E to 110.4°E. Svalbard Islands section, identified as Leg III, is from 2:00 on August 17th to 11:00 on August 19th, 2017, with latitudes from 82.6°N to 74.3°N and longitudes from 25.4°E to 2.1°E. Norwegian Sea and Iceland section, referred to as Leg IV, occurs from 14:00 on August 23rd to 14:00 on August 25th, 2017, spanning from 67.0°N to 61.2°N and from 2.1°W to 25.8°W. Atlantic Ocean section, labeled as Leg V, spanning from 14:00 on August 25th to 17:00 on August 27th, 2017, covers from 61.1°N to 56.2°N and from 25.9°W to 46.9°W.

**Figure 2.** Spectra of various types of black carbon particles with peaks displaying strong signals highlighted in blue. The X-axis represents the mass-to-charge ratio (m/z), and the Y-axis shows the relative peak area. The cation spectrum is presented in the upper half of each map, while the anion spectrum is depicted in the lower half. (a) Spectra of K-CN black carbon particles; (b) Spectra of Ca-$NO_3$ black carbon particles; (c) Spectra of K-Ni-$SO_4$ black carbon particles; (d) Spectra of $SO_4$ black carbon particles; (e) Spectra of K-$SO_4$ black carbon particles; (f) Spectra of K-lev black carbon particles.

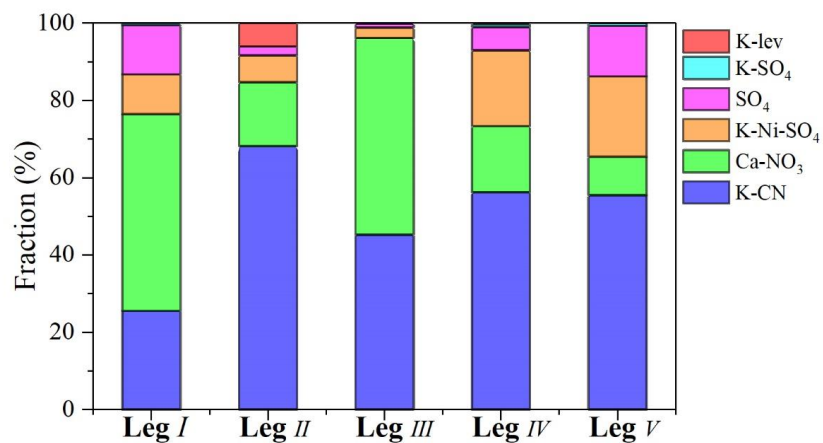**Figure 3.** Box plots of hourly counts (in red) and fractions (in blue) of black carbon particles from Leg I to Leg V. The tops and bottoms of the boxes indicate the upper and lower quartile values, respectively. Horizontal lines within the boxes denote median values. Hollow squares and dotted black lines represent mean values. Vertical whiskers extend to scattered values above and below the boxes, with caps on the whiskers indicating maximum and minimum values. Cross symbols mark the 99th and 1st percentile values, respectively.
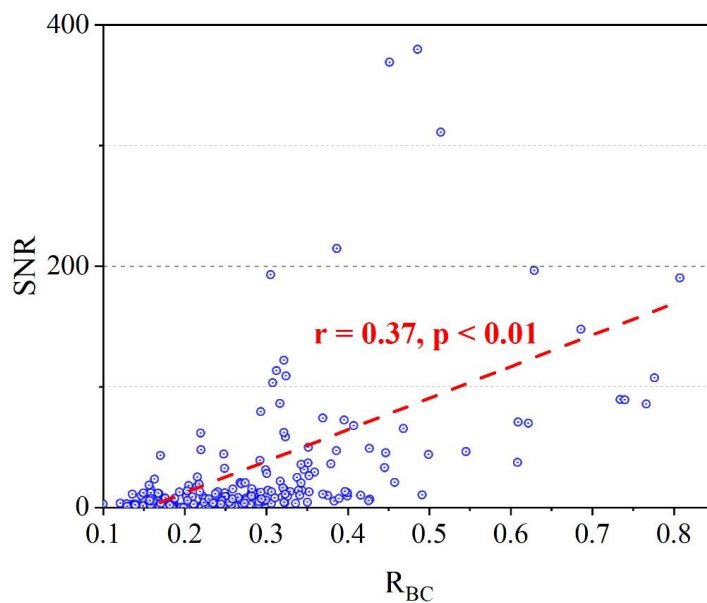
**Figure 4.** Fraction of each type of black carbon particles from Leg I to Leg V. Different colors represent various types of black carbon particles: blue for K-CN, green for Ca-NO$_3$, orange for K-Ni-SO$_4$, magenta for SO$_4$, cyan for K-SO$_4$, and red for K-lev.
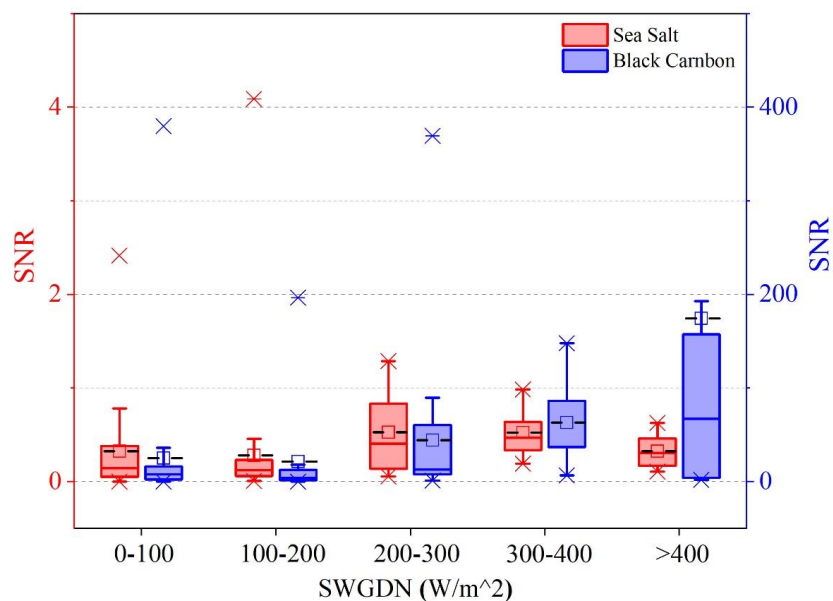
664

**Figure 5.** Correlation of SNR and $R_{BC}$ in black carbon particles. A red dashed line indicates the linear fit

curve, with the correlation coefficient (r) and significance level (p) provided.

**Figure 6**. Box plots of SNR for sea salt particles (in red) and black carbon particles (in blue), grouped by SWGDN. The upper and lower parts of the boxes indicate the quartile values, while the horizontal lines within the boxes denote the median values. Hollow squares and black dotted lines show the mean values. Vertical whiskers extend to capture scattered values above and below the boxes, with caps on the whiskers indicating the maximum and minimum values. Cross symbols mark the 99th and 1st percentile values, respectively.